



Version: V0.4  
Primary author(s): Tulika Bose, Meenakshi Narain

Send comments to [d0-run2eb-024@fnal.gov](mailto:d0-run2eb-024@fnal.gov)

## Search for $W'$ boson production in the top quark decay channel

Tulika Bose, Meenakshi Narain  
*Brown University*

E. Boos, V. Bunichev, L. Dudko, M. Perfilov  
*Moscow State University*  
(Dated: March 10, 2008)

We present the results of a search for the production of a heavy gauge boson  $W'$  using  $\sim 0.9 \text{ fb}^{-1}$  of data collected by the DØ detector. We study three different models of  $W'$  boson production using the decay channel  $W' \rightarrow t\bar{b}$ . We find no significant excess in the final state invariant mass distribution and set 95% confidence level upper limits on the production cross section. For a left-handed  $W'$  boson with SM couplings we include the interference with the SM s-channel single top quark process and set a lower mass limit of 775 GeV. For right-handed  $W'$  bosons we set lower mass limits of 785 GeV for the case  $M(\nu_R) < M(W'_R)$  and 810 GeV for  $M(\nu_R) > M(W'_R)$ . We also set constraints on the coupling to fermions as a function of  $W'$  mass.

## I. INTRODUCTION

New charged massive bosons usually called  $W'$  are predicted by various extensions of the Standard Model (SM). Such models like Non-Commuting Extended Technicolor [1], Composites [2, 3] and Little Higgs models [4–6], models of composite gauge bosons [7], Grand Unification [8] and Superstring theories [9–11] represent examples in which the extension of the gauge group leads to the appearance of a  $W'$  boson. Physical properties and interaction parameters of  $W'$  bosons can vary from model to model. For example, the  $W'$  in models of Universal extra-dimensions [12, 13] represents the lightest Kaluza-Klein mode of a charged gauge  $W^\pm$  boson and its interactions with fermion fields has the same (V-A) chiral structure as the SM  $W^\pm$  boson. In top-flavor models the  $W'$  boson interacts differently with fermions of the first two generations and with fermions of the third generation, depending on the magnitude of gauge coupling parameters  $g_h$  and  $g_l$ . If  $g_h > g_l$  the  $W'$  couples stronger to the third generation and weaker to the first two generations, and vice versa if  $g_h < g_l$  [14, 15]. Frequently  $W'$  bosons are discussed in connection with so-called Left-Right symmetric models [16–22]. The simplest extension of the SM with Left-Right symmetry is based on the  $U(1) \times SU(2)_L \times SU(2)_R$  gauge group. The left-handed fermions transform as doublets under  $SU(2)_L$  and are invariant under  $SU(2)_R$  contrary to the right-handed ones which transform as doublets under  $SU(2)_R$  and are invariant under  $SU(2)_L$ . Linear combinations of charged gauge fields produce massive eigenstates:  $W_1 = \cos \zeta W_L + \sin \zeta W_R$ ,  $W_2 = -\sin \zeta W_L + \cos \zeta W_R$ , where  $W_1$  is identified with the  $W$  boson that we know, and  $W_2$  with a new  $W'$  boson and  $\zeta$  is a mixing parameter between bosons of the right and left gauge groups. The parameter  $\zeta$  must be very small ( $\zeta < 10^{-3}$ ) to suppress (V+A) charged currents for light SM fermions in accord with experimental data [23, 24]. In this case, interactions of the  $W'$  boson with fermions becomes almost purely right-handed. In Left-Right symmetric models parity is broken spontaneously which leads to different masses for the  $SU(2)_L$  and  $SU(2)_R$  gauge bosons. There are two variants of Left-Right symmetric models, called *manifest* and *pseudo-manifest* [22] for which the Cabibbo-Kobayashi-Maskawa matrices are  $V^L = V^R$  and  $V^L = V^{R*}$ , respectively.

Although no  $W'$  boson has been discovered yet, there are experimental limits on its mass. Various models with  $W'$  bosons contain many parameters, and indirect constraints on the mass of  $W'$  bosons are highly model dependent. Indirect limits on  $W'$  bosons being extracted from leptonic and semileptonic decays and also from cosmological and astrophysical data give a very wide range of upper limits on the  $W'$  mass varying from 549 GeV up to 23 TeV [25].

Direct limits on  $W'$  masses are based on the hypotheses of a  $W'$  boson that has purely right-handed or purely left-handed interactions with SM-like coupling constants. The limits from direct searches in leptonic decay modes depend on the mass of a hypothetical right-handed neutrino. If  $M(W') < M(\nu_R)$  the decay  $W'_R \rightarrow \nu_R, \ell$  is kinematically not allowed. In this case, the limit based on decays to pairs of light quarks and antiquarks is  $M(W') > 800$  GeV [26]. If  $M(W') > M(\nu_R)$  the decay  $W' \rightarrow \nu_R, \ell$  is allowed, and the limit is  $M(W') > 786$  GeV [27] from the leptonic decay modes in both electron and muon channels.

One of the most promising ways to search for a  $W'$  boson is in decays to third generation quarks ( $W' \rightarrow t\bar{b}$ ). This channel has relatively small QCD backgrounds, compared to the decay to light quarks, and it is less model dependent. Searches in this channel at the Tevatron give the limit  $M(W') > 536$  GeV at 95% CL, assuming  $M(W') > M(\nu_R)$ . The assumption  $M(W') < M(\nu_R)$  leads to the slightly higher limit  $M(W') > 566$  GeV [28] due to the absence of leptonic decays and the correspondingly larger decay branching fraction to  $t\bar{b}$ . A  $W'$  boson that decays to  $t\bar{b}$  contributes to single-top production [29]. Since the standard model  $W$  boson and a  $W'$  boson with left-handed couplings both contribute to single-top production and couple to the same fermion multiplets they interfere with each other. The interference term may contribute as much as 16-33% of the total rate, depending on the  $W'$  mass and its couplings [30].

The most recent  $D\bar{O}$  analysis [31], taking into account the interference effect excludes masses between 200 GeV and 610 GeV for a  $W'$  boson with standard-model-like couplings, between 200 GeV and 630 GeV for a  $W'$  boson with right-handed couplings that is allowed to decay to both leptons and quarks, and between 200 GeV and 670 GeV for a  $W'$  boson with right-handed couplings that is only allowed to decay to quarks.

In this note, we present an analysis of events with the final state signature  $\ell\nu$ +jets, which follows the previously published analysis [31]. Here we extend the published analysis by i) adding about a factor of four more integrated luminosity, ii) including of searches for  $W'_L$  when no interference with SM is allowed, and iii) additionally derive limits on right and left handed gauge couplings.

## II. THE $D\bar{O}$ DETECTOR

The  $D\bar{O}$  detector is a typical multipurpose collider detector, that consists of central tracking, calorimeter, and muon detection systems. It is described in detail in Ref. [32]

The magnetic central-tracking system is comprised of a silicon microstrip tracker and a scintillating fiber tracker, both located within a 2 T superconducting solenoidal magnet. Central and forward preshower detectors are located

just outside of the coil and in front of the calorimeters. The liquid-argon/uranium calorimeter is divided into a central section covering  $|\eta| \leq 1.1$  and two end calorimeters extending coverage to  $|\eta| \leq 4$ . In addition to the preshower detectors, scintillators between the calorimeter cryostats provide sampling of developing showers at  $1.1 < |\eta| < 1.4$ . The muon system is located outside the calorimeter and consists of a layer of tracking detectors and scintillation trigger counters in front of 1.8 T toroids, and of two similar layers outside the toroids. Tracking at  $|\eta| < 1$  relies on 10 cm wide drift tubes [33], and 1 cm mini-drift tubes are used at  $1 < |\eta| < 2$ .

The trigger and data acquisition systems are designed to accommodate the high luminosities of Run II. Based on information from tracking, calorimeter, and muon systems, the output of the first level of the trigger is used to limit the rate for accepted events to  $\approx 1.5$  kHz. At the next trigger stage, with more refined information, the rate is reduced further to  $\approx 800$  Hz. These first two levels of triggering rely mainly on hardware and firmware. The third and final level of the trigger, with access to all the event information, uses software algorithms and a computer farm to reduce the output rate to  $\approx 50$  Hz, which is written to tape.

### III. DATA AND EVENT SELECTION

The data sample and event selections used for this analysis are identical to those used by the published single top quark evidence analysis [34]. There are two differences in the final selection of events. We keep events with two and three jets. The published analysis [34] also includes events with four jets. We also select events with an invariant mass constructed from the leading two jets, lepton and neutrino,  $\sqrt{\hat{s}}$ , greater than 400 GeV.

The integrated luminosity corresponding to this data sample is about  $0.9 \text{ fb}^{-1}$ . The data were recorded between August 2002 and December 2005. Reconstruction of the data was performed using version p17.09.03 of the reconstruction software. In addition the top\_cafe software version v00-08-07 in p18.08.00 was used for the analysis of the reconstructed data set. For completeness, we reproduce the list of triggers, object definitions and selection criterion used for this analysis below from Ref [35].

The data were collected using triggers that required an electron or a muon and jets. Table I summarizes the triggers used and the associated integrated luminosity for the  $e$ +jets and  $\mu$ +jets event samples.

Trigger Version	$e$ +jets channel		$\mu$ +jets channel	
	Trigger Name	$\int \mathcal{L} dt$	Trigger Name	$\int \mathcal{L} dt$
v8.0 – v9.0	EM15_2JT15	5 pb $^{-1}$	MU_JT20_L2M0	6 pb $^{-1}$
v9.0 – v10.0	EM15_2JT15	25 pb $^{-1}$	MU_JT20_L2M0	25 pb $^{-1}$
v10.0 – v11.0	EM15_2JT15	10 pb $^{-1}$	MU_JT20_L2M0	11 pb $^{-1}$
v11.0 – v12.0	EM15_2JT15	63 pb $^{-1}$	MU_JT20_L2M0	65 pb $^{-1}$
v12.0 – v13.0	E1_SHT15_2J20	227 pb $^{-1}$	MU_JT25_L2M0	231 pb $^{-1}$
v13.0 – v13.2	E1_SHT15_2J_J25	55 pb $^{-1}$	MUJ2_JT25	31 pb $^{-1}$
v13.2 – v13.3	“	“	MUJ2_JT25_LM3	16 pb $^{-1}$
v13.3 – v14.0	E1_SHT15_2J_J30	294 pb $^{-1}$	MUJ2_JT30_LM3	252 pb $^{-1}$
v14.0 – v14.2	“	“	MUJ1_JT25_LM3	0 pb $^{-1}$
v14.2 – v14.3	“	“	MUJ1_JT25_ILM3	21 pb $^{-1}$
v14.3 – v15.0	E1_SHT15_2J_J25	234 pb $^{-1}$	MUJ1_JT35_LM3	214 pb $^{-1}$
Total		913 pb $^{-1}$		871 pb $^{-1}$

TABLE I: Integrated luminosities by trigger version for the data sample.

The event selection uses the following objects.

- Primary vertices reconstructed used an adaptive algorithm [36].
- Electrons are clusters of energy depositions in the central calorimeter ( $|\eta^{\text{det}}| < 1.1$ ) with at least 90% of their energy in the electromagnetic calorimeter. They must be isolated so that  $(E_{\text{total}}(\Delta R < 0.4) - E_{\text{EM}}(\Delta R < 0.2))/E_{\text{EM}}(\Delta R < 0.2) < 0.15$ . The  $\chi^2$  from the  $7 \times 7$  H-matrix must be less than 50 to ensure that the shower profile agrees with that expected from an electromagnetic shower. The calorimeter cluster must be matched with a charged particle track with  $p_T > 5$  GeV. Electrons with these qualities are labeled “loose”. A tight isolated electron must in addition have  $L > 0.85$  for the seven-variable EM-likelihood.
- Muons are identified as tracks in the muon spectrometer and the central tracker [37]. Loose isolated muons must be of medium  $|nseg| = 3$  quality. For cosmic ray rejection we require  $|\Delta t_A| < 10$  ns and  $|\Delta t_{BC}| < 10$  ns. The track in the muon system must match a track in the central tracker with  $\chi^2/ndof < 4$  and a distance of

closest approach to the primary vertex  $< 0.2$  mm. Loose muons must be isolated from jets by  $\Delta R > 0.5$ . Tight isolated muon satisfy additional isolation criteria applied on the energy in calorimeter and the total momenta of tracks, in a cone around the muon. More details can be found in [34].

- Jets are reconstructed from energy deposits in the calorimeter using the Run II cone algorithm [38]. The certified preliminary p17 jet energy scale corrections (JetCorr v07-01-02) are applied to correct jet energies to the particle-level [39]. Jets containing a muon with  $\Delta R < 0.5$  with the jet axis are corrected for the momentum carried away by the muon and the neutrino, assuming semileptonic  $b$  or  $c$ -decay. We accept jets with  $p_T > 15$  GeV and  $|\eta| < 3.4$  that pass the jet id cuts from Ref. [40]. Monte Carlo jets are corrected for different reconstruction and identification efficiency, for the worse energy resolution, and for different calorimeter responses. The standard “jet shifting, smearing, and removal algorithm” (JSSR)[41] is applied with shifting to correct for the mean transverse energy imbalance turned off.
- $b$ -Jets are identified using lifetime tagging. Jets are first required to be “taggable”. Taggable jets are then “tagged” by the neural network tagger [42] for the data. In the MC samples, taggable  $b$ ,  $c$  and light quark jets are weighted by their respective probability to be tagged by the neural network tagger. For this analysis, we use the NN TIGHT operating point, which requires the NN output to be greater than 0.775. The average fake rate for this operating point is 0.47% and its average  $b$ -tagging efficiency is 47% for jets with  $|\eta| < 2.5$ .
- Missing  $p_T$  is computed by adding up vectorially the transverse energies in all cells of the electromagnetic and the hadronic calorimeters. Cells in the coarse hadronic calorimeter are only added if they are part of jets passing jet-id criteria. This raw quantity is then corrected for the energy corrections applied to the reconstructed objects and for the momentum of all muons in the event, corrected for their energy loss in the calorimeter.

We select events with an isolated lepton and missing transverse momentum which are likely to originate from the leptonic decay of a  $W$  boson. We consider events with two to three jets of which at least one is tagged as a  $b$ -jet.

The common selection for both electron and muon channels is:

- Good quality [43] (for data)
- Pass trigger: offline electrons and muons in the data are matched to the object that fired the appropriate trigger for that run period and triggerlist
- Good primary vertex:  $|z_{PV}| < 60$  cm with at least three tracks attached
- Missing transverse momentum  $15 < \cancel{E}_T < 200$  GeV
- Between one and three jets with  $p_T > 15$  GeV and  $|\eta| < 3.4$
- The leading jet has  $p_T > 25$  GeV and  $|\eta| < 2.5$
- The second leading jet is required to have  $p_T > 20$  GeV
- There must be fewer than three noise jets. A noise jet is defined as a jet with  $p_T > 15$  GeV, failing the jet ID, and not overlapping with a loose electron.
- Jet triangle cut  $|\Delta\phi(\text{leading jet}, \cancel{E}_T)|$  vs.  $\cancel{E}_T$ : from 1.5 to  $\pi$  if  $\cancel{E}_T = 0$  GeV, and  $\cancel{E}_T$  from 0 to 35 GeV if  $|\Delta\phi| = \pi$

The electron channel selection is:

- Only one tight electron with  $E_T > 15$  GeV and  $|\eta^{\text{det}}| < 1.1$
- No second loose electron with  $E_T > 15$  GeV
- No tight muon with  $p_T > 18$  GeV and  $|\eta^{\text{det}}| < 2.0$
- The electron comes from the primary vertex:  $|\Delta z(e, PV)| < 1$  cm
- Electron triangle cuts  $|\Delta\phi(e, \cancel{E}_T)|$  vs.  $\cancel{E}_T$ :
  - from 2 to 0 if  $\cancel{E}_T = 0$  GeV, and  $\cancel{E}_T$  from 0 to 40 GeV if  $|\Delta\phi| = 0$
  - from 1.5 to 0 if  $\cancel{E}_T = 0$  GeV, and  $\cancel{E}_T$  from 0 to 50 GeV if  $|\Delta\phi| = 0$
  - from 2 to  $\pi$  if  $\cancel{E}_T = 0$  GeV, and  $\cancel{E}_T$  from 0 to 24 GeV if  $|\Delta\phi| = \pi$

The muon channel selection is:

- Only one tight muon with  $p_T > 18$  GeV and  $|\eta^{\text{det}}| < 2.0$

- No tight electron with  $p_T > 15$  GeV and within  $|\eta^{\text{det}}| < 2.5$
- The muon comes from the primary vertex:  $|\Delta z(\mu, \text{PV})| < 1$  cm
- Muon triangle cuts  $|\Delta\phi(\mu, \cancel{E}_T)|$  vs.  $\cancel{E}_T$ :
  - from 1.1 to 0 if  $\cancel{E}_T = 0$  GeV, and  $\cancel{E}_T$  from 0 to 80 GeV if  $|\Delta\phi| = 0$
  - from 1.5 to 0 if  $\cancel{E}_T = 0$  GeV, and  $\cancel{E}_T$  from 0 to 50 GeV if  $|\Delta\phi| = 0$
  - from 2.5 to  $\pi$  if  $\cancel{E}_T = 0$  GeV, and  $\cancel{E}_T$  from 0 to 30 GeV if  $|\Delta\phi| = \pi$

#### IV. SIGNAL AND BACKGROUND MODELING

The most general, model independent, lowest order (ignoring possible higher dimension effective operators) effective interaction Lagrangian of the  $W'$  boson to SM fermions can be written as

$$\mathcal{L} = \frac{V_{f_i f_j}}{2\sqrt{2}} g_w \bar{f}_i \gamma_\mu (a_{f_i f_j}^R (1 + \gamma^5) + a_{f_i f_j}^L (1 - \gamma^5)) W' f_j + \text{H.c.}, \quad (1)$$

where  $a_{f_i f_j}^R, a_{f_i f_j}^L$  are the left and right-handed couplings of the  $W'$  boson to fermions,  $g_w = e/(s_w)$  is the SM weak coupling constant and  $V_{f_i f_j}$  is the SM CKM matrix element if the fermion ( $f$ ) is a quark, and  $V_{f_i f_j} = \delta_{ij}$  if it is a lepton, where  $\delta_{ij}$  is the Kronecker delta and  $i, j$  is the generation number. The notations are taken such that for so-called SM-like  $W'$   $a_{f_i f_j}^L = 1$  and  $a_{f_i f_j}^R = 0$ .

This effective Lagrangian has been incorporated into the CompHEP package [44] as a new theoretical model and has also been included for the purpose of event generation into the SINGLETOP generator [45]. SINGLETOP is used to simulate both the SM  $s$ - and  $t$ -channel single top backgrounds and the  $s$ -channel  $W'$  signal including interference with the standard model  $W$  boson. In all cases, we simulate the complete chain of  $W'$ , top quark, and SM  $W$  boson decays taking into account finite widths and all spin correlations between resonance state production and subsequent decay. The top quark mass,  $M_t$  is chosen to be 175 GeV. The CTEQ611 parton distribution functions are used and the QCD scale is set to  $M_{W'}$ . Next-to-Leading-Order (NLO) corrections are included in the SINGLETOP generator and normalization and matching between various partonic sub-processes are performed such that not only NLO rates, but also the NLO shapes of distributions are reproduced [46],- [50].

In order to simulate the general coupling dependence it is useful to study MC samples for different cases separately [30]: samples of  $W'$  bosons with purely left-handed couplings and samples of  $W'$  bosons with purely right-handed couplings. For all generated signal samples the following nomenclature is used:

- “SM+ $W'_L$ ” i.e.  $a_{ud}^L = a_{cs}^L = a_{tb}^L = 1$ ,  $a_{ud}^R = a_{cs}^R = a_{tb}^R = 0$ ,
- “ $W'_R$ ” i.e right-handed  $W'$  with  $a_{ud}^L = a_{cs}^L = a_{tb}^L = 0$ ,  $a_{ud}^R = a_{cs}^R = a_{tb}^R = 1$ .

The differences between  $W'$  bosons with left- and right-handed couplings that are relevant for our search are that  $W'_L$  bosons which have left-handed couplings couple to the same fermion multiplets as the standard  $W$  boson and therefore there will be interference between the two  $tb$  production diagrams with a  $W$  boson and with a  $W'_L$  boson. These  $W'_L$  bosons decay to the same final states as the standard  $W$  boson.  $W'_R$  bosons with purely right-handed couplings couple to different final state particles and therefore do not interfere with the standard  $W$  boson. Since their leptonic decays involves a right-handed neutrino  $\nu_R$  of unknown mass they may only be allowed to decay to  $q\bar{q}'$  final states, if  $M_{\nu_R} > M_{W'}$ , or they may decay to  $\ell\nu$  and  $q\bar{q}'$  final states, if  $M_{\nu_R} < M_{W'}$ , leading to different branching fractions for  $W' \rightarrow tb$ . In the absence of interference between  $W$  and  $W'$  and if  $M_{\nu_R} < M_{W'}$ , there is no difference between  $W'_L$  and  $W'_R$  for our search.

The  $W'$  width depends on how many decay modes are open. If  $M_{\nu} > M_{W'}$  and only  $q\bar{q}'$  final states are open the width will be smaller than if  $\ell\nu$  and  $q\bar{q}'$  final states are open. The expected LO widths of  $W'$  bosons are listed in Table II [30]. NLO corrections are of the order of 5% [46].

Figure 1 (top) shows the invariant mass distribution for the different cases of production of a  $W'$  boson with mass 700 GeV at the parton level. The distributions for both the left- and right-handed  $W'$  show a resonant structure around 700 GeV. However, for the left-handed  $W'$  bosons (the red curve, also denoted as SM+ $W'_L$ ), we note that there is a minimum corresponding to destructive interference between the SM  $W$  boson and the  $W'_L$  boson contributions. The same figure also shows that the shape of the invariant mass peak does not depend much on the allowed decay modes of the right-handed  $W'$  boson ( $W' \rightarrow \ell\nu$  or  $q\bar{q}'$  vs.  $W' \rightarrow q\bar{q}'$  only). The distributions have the same shape, only the normalizations are different. Figure 1(bottom) shows the invariant mass distribution for a “mixed”  $W'$  boson that has left- as well as right-handed couplings. Here again no difference in shape is observed for the different decays. Therefore, for the purpose of this analysis we generate two main categories of event samples:

$M_{W'}$ [GeV]	$\Gamma_{W'} [GeV]$	
	$M_\nu < M_{W'}$	$M_\nu > M_{W'}$
600	19.7	14.6
650	21.4	15.9
700	23.1	17.2
750	24.9	18.5
800	26.6	19.8
850	28.3	21.1
900	30.0	22.4

TABLE II: Total width of the  $W'$  as a function of the assumed mass.

$M_{W'}$ (GeV)	$\sigma(W'_L) \times BR(W'_L \rightarrow tb)$ (pb)	$\sigma(W'_R) \times BR(W' \rightarrow tb)$	
		$M_{\nu_R} < M_{W'}$ (pb)	$M_{\nu_R} > M_{W'}$ pb
600	2.17 ( $\pm 11\%$ )	2.10 ( $\pm 11\%$ )	2.79 ( $\pm 11\%$ )
650	1.43 ( $\pm 13\%$ )	1.25 ( $\pm 13\%$ )	1.65 ( $\pm 12\%$ )
700	1.01 ( $\pm 13\%$ )	0.74 ( $\pm 13\%$ )	0.97 ( $\pm 13\%$ )
750	0.76 ( $\pm 14\%$ )	0.44 ( $\pm 14\%$ )	0.57 ( $\pm 14\%$ )
800	0.62 ( $\pm 15\%$ )	0.26 ( $\pm 15\%$ )	0.34 ( $\pm 15\%$ )
850	0.55 ( $\pm 16\%$ )	0.16 ( $\pm 16\%$ )	0.20 ( $\pm 16\%$ )
900	0.51 ( $\pm 17\%$ )	0.09 ( $\pm 17\%$ )	0.12 ( $\pm 18\%$ )

TABLE III: List of signal samples and total NLO cross sections for the process  $p\bar{p} \rightarrow \sigma(W') \times BR(W' \rightarrow tb)$ . The uncertainty includes contributions from scale, PDFs, and the top quark mass.

- (a) Left-handed  $W'$  boson with the interference term included ( $W'_L$ ),
- (b) Right-handed  $W'$  boson with all decays of the  $W'$  allowed. The only relevant difference with a  $W'$  that decays only to  $qq'$  is the branching fraction to  $tb$ .

$W'$  bosons with masses below 600 GeV have been ruled out [31]. In order to extend the limit to higher masses we simulate  $W'$  bosons at seven mass values from 600 to 900 GeV, separately for  $W'$  bosons with purely right- and purely left-handed interactions.

Table III shows the NLO production cross-sections for a  $W'$  boson with SM-like couplings ( $W'_L$ ) and also for a  $W'$  boson with right-handed couplings ( $W'_R$ ). The  $W'_L$  cross-section takes into account both the  $s$ -channel SM  $W$  diagram and the  $s$ -channel  $W'$  diagram and the interference between the two. The factorization scale is set to the  $W'$  boson invariant mass for the generation of the COMPHEP samples and also to compute the leading order cross-section. The LO cross-section is then scaled to NLO using  $k$ -factors based on Ref. [46]. The uncertainties quoted in Table III include contributions from scale, PDFs, and top quark mass ( $\pm 5$  GeV). The NLO cross-sections for the  $W'$  boson with pure right-handed couplings,  $W'_R$ , are taken directly from Ref. [46] since there is no interference term.

These parton-level samples are then processed with PYTHIA [51] and a GEANT [52]-based simulation of the DØ detector, and the resulting lepton and jet energies are smeared to reproduce the resolutions observed in data. Background yields are estimated using both Monte Carlo samples and data. The procedure followed is identical to that used in Ref.[34]. The  $W$ +jets background is estimated using Monte Carlo events generated with ALPGEN [53]. The overall  $W$ +jets yield is normalized to the data sample before requiring a  $b$ -tagged jet, and the fraction of heavy flavor ( $Wb\bar{b}$ ,  $Wc\bar{c}$ ) events is obtained from data. The di-boson ( $WW$  and  $WZ$ ) backgrounds are implicitly included in the background model because we normalize the  $W$ +jets background to data and are expected to be small. The  $t\bar{t}$  background is estimated using Monte Carlo samples generated with ALPGEN, normalized to the (N)NLO cross section calculation:  $\sigma(t\bar{t}) = 6.8 \pm 1.2\text{pb}$  [54]. Finally, data events with fake leptons are used to model the multijet background in which a jet is misidentified as an electron, or a muon in a jet from  $b$ -decay is misidentified as a muon from the decay of a  $W$  boson.

## V. ANALYSIS

We are searching for the  $W'$  decay chain  $W' \rightarrow tb \rightarrow Wbb \rightarrow \ell\nu bb$  using  $\ell\nu$ +jet events. The distinguishing feature of a  $W'$  signal is a narrow resonance structure in the  $tb$  invariant mass. However, We cannot directly measure the

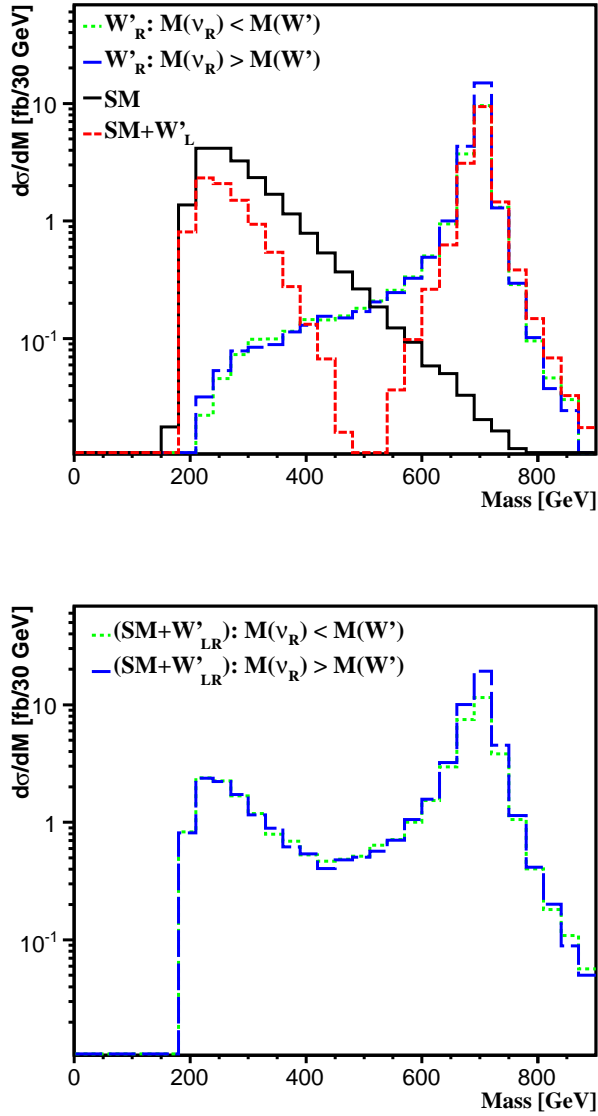


FIG. 1: Parton level invariant mass distributions for the different categories of  $W'$  boson production with a mass of 700 GeV.

$tb$  invariant mass. Instead we reconstruct the invariant mass if the leading two jets, the charged lepton and the neutrino,  $\sqrt{\hat{s}}$ , by adding their measured four-momentum vectors. The missing transverse energy is used to obtain the  $xy$ -components of the neutrino momentum and the  $z$ -component is calculated using a  $W$  boson mass constraint and choosing the solution with the minimum  $|p'_z|$  from the two possible solutions.

Figure 2 shows the reconstructed  $\sqrt{\hat{s}}$  distribution for two different simulated  $W'$  mass values (700 and 800 GeV). Also included in the plot are the main background contributions. The plot shows that the background contributions peak at smaller invariant masses ( $< 400$  GeV) while the signal distributions exhibit two peaks for  $W'_L$ . The peak at the lower end is due to the contribution from the SM  $W$  boson while the peak at the higher end is at the invariant mass of the  $W'$  boson. The relative height difference between the two peaks is directly related to the weight of the SM  $s$ -channel and  $W'_L$  contributions and depends on the mass of the  $W'_L$ . A cut on  $\sqrt{\hat{s}} > 400$  GeV is applied to the SM backgrounds and define the  $W'$  signal enriched region. As mentioned earlier  $\sqrt{\hat{s}}$  is the invariant mass formed using the lepton, neutrino and the leading two jets in the event.

The number of signal and background events after basic selection are listed in Tables IV and V. We only use events with  $\sqrt{\hat{s}} > 400$  GeV to search for a  $W'$  signal or set limits on its production, as the case may be. The numbers

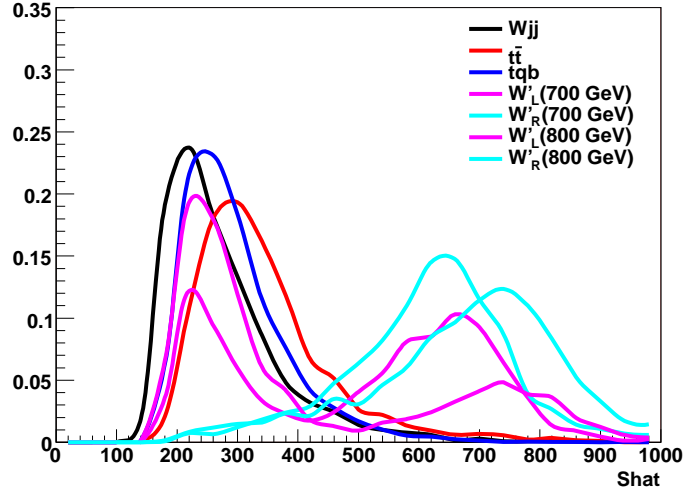


FIG. 2: Reconstructed  $W'$  invariant mass distributions for two signal mass points and also for the background processes. The distributions are normalized to unit area.

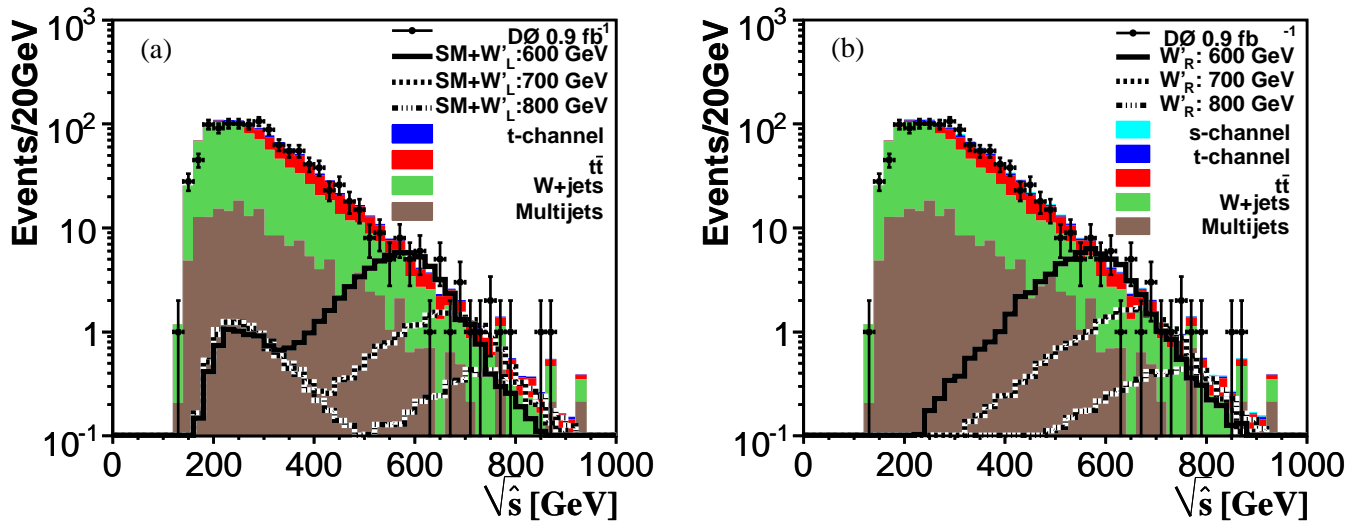


FIG. 3: Reconstructed  $W'$  invariant mass distributions for the data, the background processes, and (a)  $W'_L$  and (b)  $W'_R$  signal at three different masses. The data presented here is a combination of all eight subsamples (electron and muon, 2 and 3 jets, 1 and 2 tags)

obtained after requiring  $\sqrt{\hat{s}} > 400$  GeV are shown in Tables VI and VII. Figure 3 shows the reconstructed  $tb$  invariant mass distribution ( $\sqrt{\hat{s}}$ ) for our data and  $W'$  signals generated at three different mass values (600, 700, and 800 GeV). Also included in the plots are the main background contributions.

We also compare the data and background distributions for the eight different sub-samples which constitute the final result: the single-tagged and double-tagged analysis channels, the muon and electron channels and the two-jet and three-jet samples. The top plots in Fig. 4 show the comparison of the invariant mass distribution in data with the sum of all background processes separately for the electron and muon channels for the single tagged sample. Also shown are the signal contributions for three different  $W'$  mass points for the left handed case. The plots for the double-tagged channel are shown in Fig. 5. Figs. 11 and 12 in appendix show the same for the right-handed  $W'$  couplings. Distributions for pretagged events (Figs. 13) can also be found in the appendix.

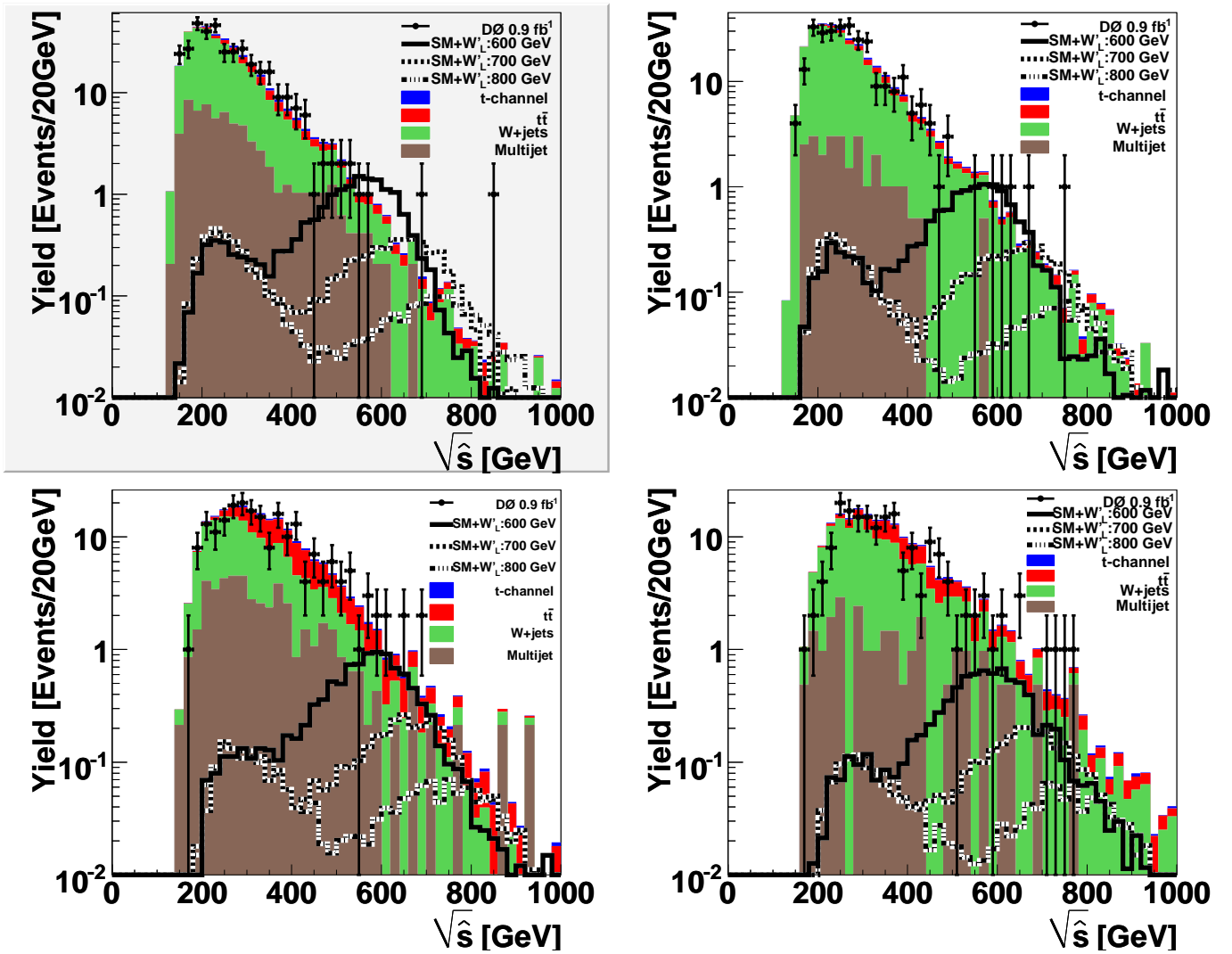


FIG. 4: Reconstructed  $W'$  invariant mass distributions for data, background and three different  $W'_L$  signal mass points for events with one  $b$ -tagged jet. The plots in the top (bottom) row are for events with two (three) jets. Events with electrons (muons) are shown on the left (right).

## VI. SYSTEMATIC UNCERTAINTIES

Systematic uncertainties were evaluated in two ways:

- Uncertainty on the normalization:  
This category includes uncertainties in the integrated luminosity, theoretical cross-sections and branching fractions, object identification efficiencies, trigger, and jet fragmentation modeling. Also included are uncertainties related to obtaining the heavy flavor ratio from data [34]. Details of these uncertainties for the signal and background samples are shown in Tables VIII – XI for both the single-tagged and double-tagged electron and muon channels with exactly two jets. The systematic uncertainties for the three-jet case are given in Tables XV– XVIII of Appendix A.
- Uncertainties that also change the shape of the distributions:  
This category includes the uncertainty in the  $b$ -tag simulation and also the uncertainty from the jet energy scale. These were evaluated by raising and lowering the tag rate and jet energy scale correction by one standard deviation and repeating the whole analysis. The average values listed in Tables VIII – XI and XV– XVIII are for illustration only.

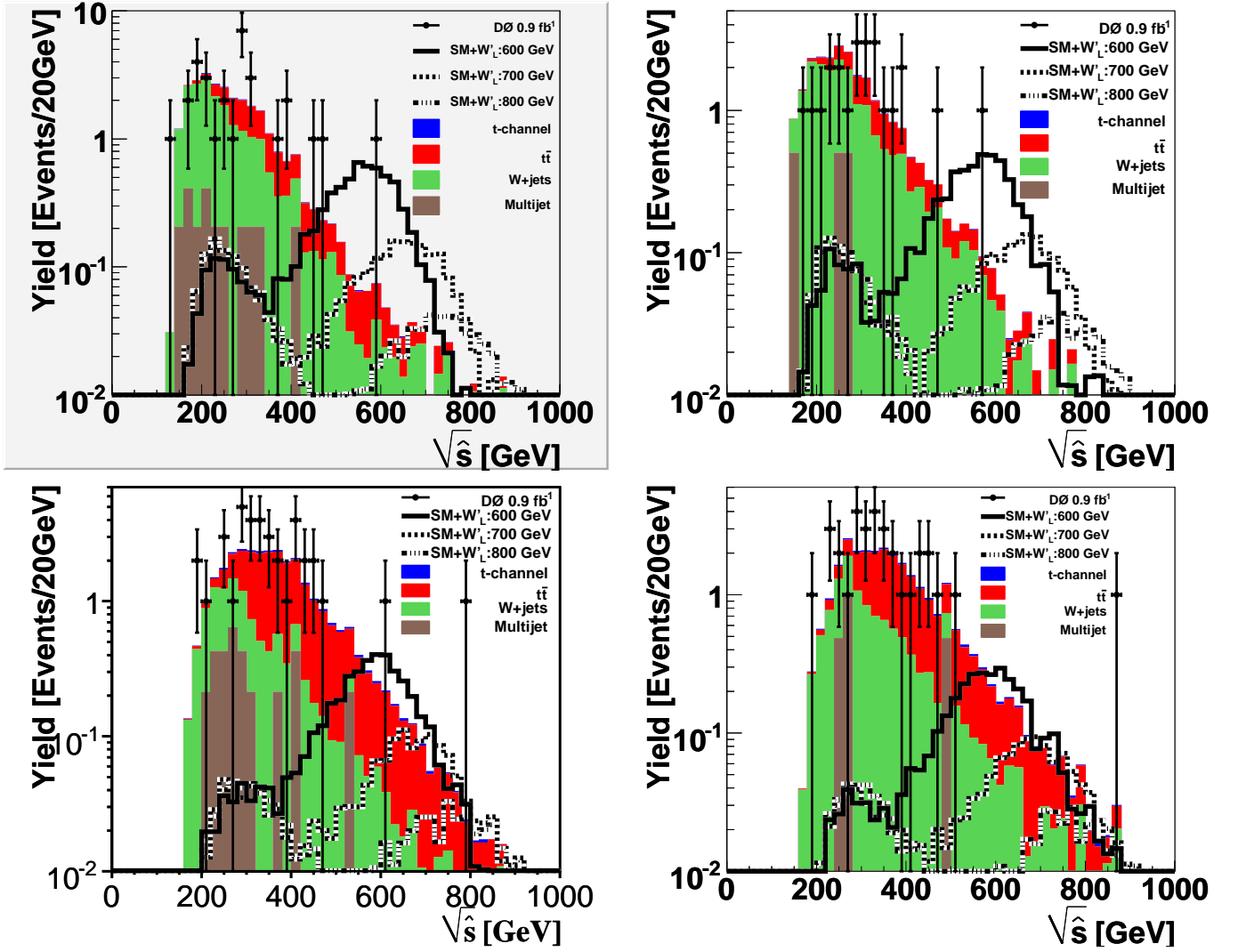


FIG. 5: Reconstructed  $W'$  invariant mass distributions for data, background and three different  $W'_L$  signal mass points for events with two  $b$ -tagged jets. The plots in the top (bottom) row are for events with two (three) jets. Events with electrons (muons) are shown on the left (right).

## VII. CROSS SECTION LIMITS

We use the distribution of the invariant mass  $\sqrt{\hat{s}}$  to discriminate signal from background. The observed data is consistent with the background predictions within uncertainties. We therefore set upper limits on the  $W'$  boson production cross section for different  $W'$  masses using the Bayesian statistics approach of the `top_statistics` package [55]. This approach employs a binned likelihood to calculate upper limits on the signal production cross section times branching fraction:  $\sigma(p\bar{p} \rightarrow W') \times \mathcal{B}(W' \rightarrow t\bar{b})$ . To obtain these limits, we combine the single-tagged and double-tagged channels, the muon and electron channels, and the two-jet and three-jet samples, a total of eight sub-samples. We bin the  $\sqrt{\hat{s}}$  invariant mass distribution in the range 400–1000 GeV into 30 bins for all the eight sub-samples. These are used as the input likelihoods. A Poisson distribution for the observed counts and a flat positive prior probability for the signal cross section are assumed. The procedure accounts for the effects on normalization and shape due to systematic uncertainties as necessary (see section VI). We also compute expected cross-section limits for each  $W'$  boson mass as a measure of the sensitivity of the analysis. Table XII shows the expected and measured cross section limits for different  $W'$  boson masses for  $W'_L$ , taking into account interference with the SM  $W \rightarrow t\bar{b}$  process. These limits are shown separately for the two-jet sample and the combined (two jet + three jet) sample. Similar limits are shown for  $W'_R$  in Table XIII. The limits in Table XIII are also applicable to a left-handed  $W'_L$  if no interference with

Yields with One $b$ -Tagged Jet				
	Electron Channel		Muon Channel	
	2 jets	3 jets	2 jets	3 jets
Left-handed signals (SM+ $W'_L$ )				
$W'$ (600 GeV)	16.5	10.4	12.3	8.1
$W'$ (650 GeV)	10.4	6.4	7.8	5.0
$W'$ (700 GeV)	7.1	4.0	5.3	3.3
$W'$ (750 GeV)	5.1	2.8	4.1	2.2
$W'$ (800 GeV)	4.2	2.1	3.2	1.8
$W'$ (850 GeV)	3.8	1.9	2.8	1.5
$W'$ (900 GeV)	3.5	1.6	2.7	1.3
Right-handed signals ( $W'_R$ )				
$W'$ (600 GeV)	15.2	9.2	13.2	8.9
$W'$ (650 GeV)	8.9	5.4	7.4	5.1
$W'$ (700 GeV)	5.0	3.1	4.2	3.0
$W'$ (750 GeV)	3.0	1.8	2.5	1.7
$W'$ (800 GeV)	1.7	1.0	1.5	1.0
$W'$ (850 GeV)	1.0	0.6	0.8	0.6
$W'$ (900 GeV)	0.6	0.4	0.5	0.3
Backgrounds				
s-channel (only for $W'_R$ )	7	3	5	2
t-channel	11	6	9	5
$t\bar{t} \rightarrow ll$	16	13	13	10
$t\bar{t} \rightarrow$ +jets	11	47	6	32
$Wb\bar{b}$	120	50	110	56
$Wc\bar{c}$	74	36	74	46
$Wjj$	61	20	58	23
Multijets	66	48	26	24
Background Sum (for $W'_L$ )	359	219	275	196
Background Sum (for $W'_R$ )	366	222	282	198
Data	357	207	287	179

TABLE IV: Yields after selection for events with exactly one  $b$ -tagged jet.

the SM is taken into account.

The observed limits, along with the theoretical cross section predictions, are shown in Figs. 6 and 7 for  $W'_L$  and  $W'_R$ , respectively. The solid line denotes the observed limit and the shaded areas above the line are excluded at 95% CL. The lower mass limit is defined by the intersection of the solid line denoting the observed limit with the dashed line for the nominal value of the theoretical cross section. For a left-handed  $W'$  boson the mass limit is 775 GeV, when interference with SM  $W \rightarrow tb$  is included. The limit is 785 GeV for a right-handed  $W'$  when  $M(\nu_R) < M(W')$  and applies also to a left-handed  $W'$  boson if no interference with the SM is taken into account. For the case  $M(\nu_R) < M(W')$ , we find  $M(W'_R) > 810$  GeV for a right-handed  $W'$  boson. The limits determined by intersecting the experimental limit curve with the nominal theory cross section prediction and with the theory cross section varied up and down by their uncertainties are listed in Table XIV.

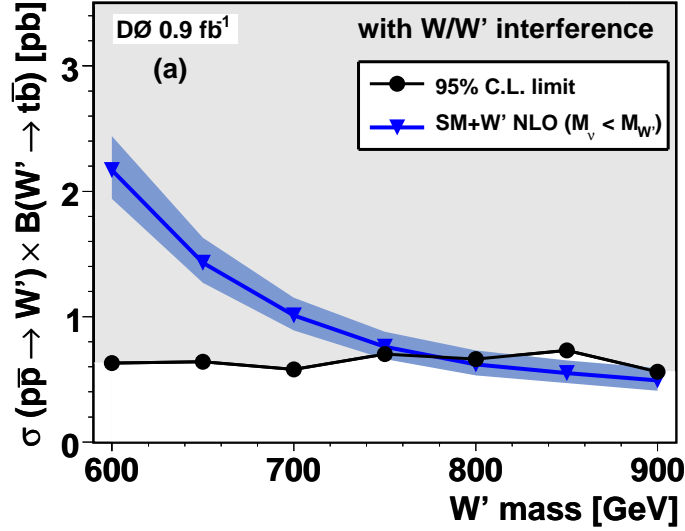
The expected limits for a left-handed  $W'$  are plotted along with the observed limits in Fig. 8. Also shown are the observed limits from Ref. [31]. Figure 9 shows the limits on both right-handed  $W'$  and left-handed  $W'$  when no interference with the SM is included. We note that our results are a significant improvement compared to the earlier published results.

### VIII. $W'$ COUPLING STRENGTH

The effective Lagrangian given by Eq. 1 can be re-written using the following form for searches that concentrate on purely left-handed or right-handed  $W'$  bosons[57]:

$$\mathcal{L} = \frac{1}{2\sqrt{2}} \bar{f}_i \gamma_\mu (g_R e^{i\omega} \cos \zeta V_{f_i f_j}^R (1 \pm \gamma_5) + g_L \sin \zeta V_{f_i f_j}^L (1 \pm \gamma_5)) W' f_j + h.c., \quad (2)$$

	Electron Channel		Muon Channel	
	2 jets	3 jets	2 jets	3 jets
Left-handed signals ( $SM+W'_L$ )				
$W'$ (600 GeV)	6.5	4.1	5.2	3.3
$W'$ (650 GeV)	4.0	2.5	3.2	2.1
$W'$ (700 GeV)	2.7	1.5	2.2	1.4
$W'$ (750 GeV)	1.9	1.1	1.6	0.9
$W'$ (800 GeV)	1.5	0.8	1.2	0.7
$W'$ (850 GeV)	1.3	0.7	1.1	0.6
$W'$ (900 GeV)	1.2	0.6	1.0	0.5
Right-handed signals ( $W'_R$ )				
$W'$ (600 GeV)	5.8	3.5	5.5	3.6
$W'$ (650 GeV)	3.3	2.1	3.1	2.1
$W'$ (700 GeV)	1.9	1.2	1.8	1.2
$W'$ (750 GeV)	1.1	0.7	1.0	0.7
$W'$ (800 GeV)	0.6	0.4	0.6	0.4
$W'$ (850 GeV)	0.4	0.2	0.4	0.2
$W'$ (900 GeV)	0.2	0.1	0.2	0.1
Backgrounds				
s-channel (only for $W'_R$ )	2.3	1.1	1.9	0.9
t-channel	0.3	0.8	0.2	0.7
$t\bar{t} \rightarrow ll$	5.5	4.6	4.6	3.8
$t\bar{t} \rightarrow +jets$	1.7	13.6	1.0	10.2
$Wb\bar{b}$	16.2	6.8	15.3	8.2
$Wc\bar{c}$	1.6	1.1	1.6	1.5
$Wjj$	0.1	0.1	0.1	0.1
Multijets	2.5	3.2	1.5	1.9
Background Sum (for $W'_L$ )	27.8	30.2	24.3	26.4
Background Sum (for $W'_R$ )	30.1	31.3	26.2	27.3
Data	30	37	23	32

TABLE V: Yields after selection for events with exactly two  $b$ -tagged jet.FIG. 6: 95% C.L. limits for  $W'$  as a function of its mass. NLO theoretical cross sections are also shown for a left-handed  $W'$  when interference effects with the SM are included. The shaded region is excluded by this analysis.

Yields with One $b$ -Tagged Jet ( $\sqrt{s} > 400$ GeV)				
	Electron Channel		Muon Channel	
	2 jets	3 jets	2 jets	3 jets
Left-handed signals ( $SM+W'_L$ )				
$W'$ (600 GeV)	13.62	9.22	10.27	7.28
$W'$ (650 GeV)	7.79	5.41	5.90	4.22
$W'$ (700 GeV)	4.40	3.01	3.36	2.57
$W'$ (750 GeV)	2.50	1.77	1.99	1.45
$W'$ (800 GeV)	1.40	1.08	1.11	0.94
$W'$ (850 GeV)	0.86	0.79	0.67	0.62
$W'$ (900 GeV)	0.58	0.50	0.46	0.44
Right-handed signals ( $W'_R$ )				
$W'$ (600 GeV)	13.94	8.74	12.04	8.48
$W'$ (650 GeV)	8.30	5.19	6.90	4.91
$W'$ (700 GeV)	4.62	3.02	3.95	2.92
$W'$ (750 GeV)	2.84	1.69	2.31	1.64
$W'$ (800 GeV)	1.53	0.94	1.36	0.95
$W'$ (850 GeV)	0.89	0.57	0.77	0.54
$W'$ (900 GeV)	0.50	0.32	0.43	0.32
Backgrounds				
s-channel (only for $W'_R$ )	0.66	0.75	0.64	0.69
t-channel	1.31	1.92	0.99	1.56
$t\bar{t} \rightarrow ll$	2.25	4.01	1.80	3.17
$t\bar{t} \rightarrow +\text{jets}$	2.19	17.07	1.37	12.63
$Wb\bar{b}$	6.51	8.51	9.53	12.38
$Wc\bar{c}$	4.22	6.03	6.49	10.19
$Wjj$	4.48	4.03	6.01	6.12
Multijets	7.79	10.84	1.50	8.21
Background Sum (for $W'_L$ )	28.75	52.41	27.69	54.26
Background Sum (for $W'_R$ )	29.41	53.16	28.33	54.95
Data	27	57	25	49

TABLE VI: Yields after selection for events with exactly one  $b$ -tagged jet and with  $\sqrt{s} > 400$  GeV.

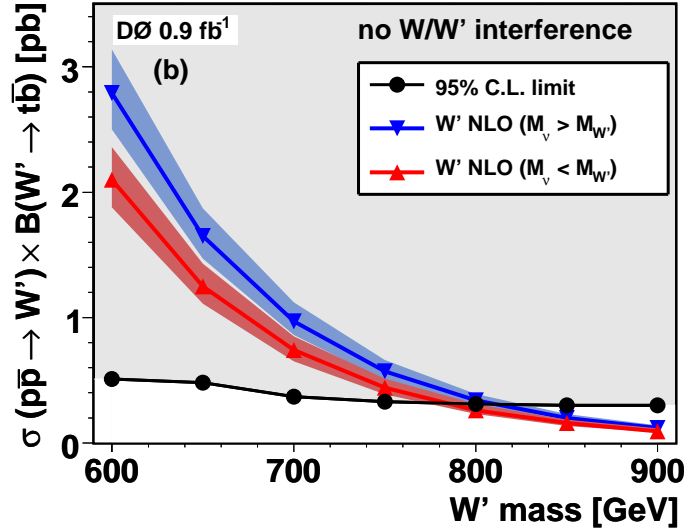


FIG. 7: 95% C.L. upper limits for  $W'$  as a function of its mass. NLO theoretical cross sections for two cases  $M(\nu_R) < M(W')$  and  $M(\nu_R) > M(W')$  are also shown. No interference with the SM is included. The shaded region is excluded by this analysis.

Yields with two $b$ -Tagged Jets ( $\sqrt{s} > 400$ GeV)				
	Electron Channel		Muon Channel	
	2 jets	3 jets	2 jets	3 jets
Left-handed signals (SM+ $W'_L$ )				
$W'$ (600 GeV)	5.6	3.7	4.5	3.0
$W'$ (650 GeV)	3.2	2.2	2.6	1.8
$W'$ (700 GeV)	1.8	1.2	1.5	1.1
$W'$ (750 GeV)	1.0	0.7	0.9	0.6
$W'$ (800 GeV)	0.6	0.4	0.5	0.4
$W'$ (850 GeV)	0.3	0.3	0.3	0.2
$W'$ (900 GeV)	0.2	0.2	0.2	0.2
Right-handed signals ( $W'_R$ )				
$W'$ (600 GeV)	5.5	3.4	5.1	3.5
$W'$ (650 GeV)	3.1	2.0	2.9	2.0
$W'$ (700 GeV)	1.8	1.2	1.7	1.2
$W'$ (750 GeV)	1.1	0.7	1.0	0.7
$W'$ (800 GeV)	0.6	0.4	0.6	0.4
$W'$ (850 GeV)	0.3	0.2	0.3	0.2
$W'$ (900 GeV)	0.2	0.1	0.2	0.1
Backgrounds				
s-channel (only for $W'_R$ )	0.3	0.3	0.3	0.3
t-channel	0.0	0.3	0.0	0.2
$t\bar{t} \rightarrow ll$	0.8	1.5	0.7	1.2
$t\bar{t} \rightarrow +\text{jets}$	0.4	5.5	0.2	4.3
$Wb\bar{b}$	1.0	1.2	1.5	1.8
$Wc\bar{c}$	0.1	0.2	0.2	0.4
$Wjj$	0.0	0.0	0.0	0.0
Multijets	0.2	0.6	0.0	0.5
Background Sum (for $W'_L$ )	2.5	9.3	2.6	8.4
Background Sum (for $W'_R$ )	2.8	9.6	2.9	8.7
Data	3	11	2	8

TABLE VII: Yields after selection for events with exactly two  $b$ -tagged jets and with  $\sqrt{s} > 400$  GeV.

	Single-Tagged Electron Channel Percentage Errors								
	$W'$	$tb$	$tqb$	$t\bar{t}l_j$	$t\bar{t}ll$	$Wb\bar{b}$	$Wc\bar{c}$	$Wjj$	Multijet
Luminosity	6.1	6.1	6.1	6.1	6.1	—	—	—	—
Cross section	—	16.0	15.0	18.0	18.0	—	—	—	—
Branching fraction	1.0	1.0	1.0	1.0	1.0	—	—	—	—
Matrix method	—	—	—	—	—	18.2	18.2	18.2	18.2
Primary vertex	2.4	2.4	2.4	2.4	2.4	—	—	—	—
Electron ID	5.5	5.5	5.5	5.5	5.5	—	—	—	—
Jet ID	1.5	1.5	1.5	1.5	1.5	—	—	—	—
Jet fragmentation	5.0	5.0	5.0	7.0	5.0	—	—	—	—
Trigger	3.0	3.0	3.0	3.0	3.0	—	—	—	—
Components for Normalization and Shape									
Jet energy scale	3.5(2.1)	1.4	0.3	9.9	1.7	—	—	—	—
Flavor-dependent TRFs	2.0(1.9)	2.1	5.9	4.6	2.4	4.4	6.3	7.4	—

TABLE VIII: Electron channel uncertainties, requiring exactly one tag and exactly two jets.  $W'$  shape uncertainties include numbers for both  $W'_R$  and  $W'_L$  (in parenthesis).

where  $\zeta$  is the left-right mixing angle,  $\omega$  is a CP-violating phase that can be absorbed into  $V^R$ , and  $g_R$  and  $g_L$  are the right and left gauge couplings, respectively. Since the leading order  $s$ -channel production process has two  $qW'q$  vertices, the total  $p\bar{p} \rightarrow W't\bar{b}$  cross-section is proportional to  $g'^4$ , where  $g'$  depends on the model being used and is either  $g_R$  or  $g_L$ . In models with non-SM couplings ( $g' \neq g_{SM}$ ) the reconstructed  $W'$  invariant mass distribution could be identical to the  $g' = g_{SM}$  case but with a normalization that differs by a factor of  $g'^4/g_{SM}^4$ . Therefore, to derive limits on the  $W'$  coupling strength we calculate the fourth root of the ratio of the experimentally excluded  $W'$

	Double-Tagged Electron Channel Percentage Errors								
	$W'$	$tb$	$tqb$	$t\bar{l}j$	$t\bar{l}l$	$Wbb$	$Wcc$	$Wjj$	Multijet
Luminosity	6.1	6.1	6.1	6.1	6.1	—	—	—	—
Cross section	—	16.0	15.0	18.0	18.0	—	—	—	—
Branching fraction	1.0	1.0	1.0	1.0	1.0	—	—	—	—
Matrix method	—	—	—	—	—	26.5	26.5	26.5	26.5
Primary vertex	2.4	2.4	2.4	2.4	2.4	—	—	—	—
Electron ID	5.5	5.5	5.5	5.5	5.5	—	—	—	—
Jet ID	1.5	1.5	1.5	1.5	1.5	—	—	—	—
Jet fragmentation	5.0	5.0	5.0	7.0	5.0	—	—	—	—
Trigger	3.0	3.0	3.0	3.0	3.0	—	—	—	—
Components for Normalization and Shape									
Jet energy scale	2.9(1.8)	0.8	4.1	8.0	1.8	—	—	—	—
Flavor-dependent TRFs	13.8(13.7)	12.9	12.9	13.5	13.0	12.2	13.6	16.1	—

TABLE IX: Electron channel uncertainties, requiring exactly two tags and exactly two jets.  $W'$  shape uncertainties include numbers for both  $W'_R$  and  $W'_L$  (in parenthesis).

	Single-Tagged Muon Channel Percentage Errors								
	$W'$	$tb$	$tqb$	$t\bar{l}j$	$t\bar{l}l$	$Wbb$	$Wcc$	$Wjj$	Multijet
Luminosity	6.1	6.1	6.1	6.1	6.1	—	—	—	—
Cross section	—	16.0	15.0	18.0	18.0	—	—	—	—
Branching fraction	1.0	1.0	1.0	1.0	1.0	—	—	—	—
Matrix method	—	—	—	—	—	20.7	20.7	20.7	20.7
Primary vertex	3.0	3.0	3.0	3.0	3.0	—	—	—	—
Muon ID	7.4	7.4	7.4	7.4	7.4	—	—	—	—
Jet ID	1.5	1.5	1.5	1.5	1.5	—	—	—	—
Jet fragmentation	5.0	5.0	5.0	7.0	5.0	—	—	—	—
Trigger	6.0	6.0	6.0	6.0	6.0	—	—	—	—
Components for Normalization and Shape									
Jet energy scale	13.1(8.8)	5.3	6.1	20.1	6.8	—	—	—	—
Flavor-dependent TRFs	1.6(1.6)	1.8	5.9	4.5	2.0	4.4	6.3	7.5	—

TABLE X: Muon channel uncertainties, requiring exactly one tag and exactly two jets.  $W'$  shape uncertainties include numbers for both  $W'_R$  and  $W'_L$  (in parenthesis).

	Double-Tagged Muon Channel Percentage Errors								
	$W'$	$tb$	$tqb$	$t\bar{l}j$	$t\bar{l}l$	$Wbb$	$Wcc$	$Wjj$	Multijet
Luminosity	6.1	6.1	6.1	6.1	6.1	—	—	—	—
Cross section	—	16.0	15.0	18.0	18.0	—	—	—	—
Branching fraction	1.0	1.0	1.0	1.0	1.0	—	—	—	—
Matrix method	—	—	—	—	—	27.6	27.6	27.6	27.6
Primary vertex	3.0	3.0	3.0	3.0	3.0	—	—	—	—
Muon ID	7.4	7.4	7.4	7.4	7.4	—	—	—	—
Jet ID	1.5	1.5	1.5	1.5	1.5	—	—	—	—
Jet fragmentation	5.0	5.0	5.0	7.0	5.0	—	—	—	—
Trigger	6.0	6.0	6.0	6.0	6.0	—	—	—	—
Components for Normalization and Shape									
Jet energy scale	12.5(9.6)	5.2	9.1	19.7	6.9	—	—	—	—
Flavor-dependent TRFs	13.7(13.4)	12.9	12.8	13.4	12.9	12.2	13.5	16.1	—

TABLE XI: Muon channel uncertainties, requiring exactly two tags and exactly two jets.  $W'$  shape uncertainties include numbers for both  $W'_R$  and  $W'_L$  (in parenthesis).

cross-section and the nominal theoretical cross-section with SM couplings. Figure 10 shows the observed limit on the ratio of  $g'/g_{SM}$ . We exclude gauge couplings above  $0.65g_{SM}$  for the case the  $W'$  boson decays to quarks only and for a  $W'$  mass of 600 GeV. Our results are comparable to those obtained by the CDF collaboration from the analysis of a dataset with comparable luminosity [56].

	$W'$ (600 GeV)		$W'$ (650 GeV)		$W'$ (700 GeV)		$W'$ (750 GeV)		$W'$ (800 GeV)		$W'$ (850 GeV)		$W'$ (900 GeV)	
	Exp.	Obs.	Exp.	Obs.	Exp.	Obs.	Exp.	Obs.	Exp.	Obs.	Exp.	Obs.	Exp.	Obs.
<u>Statistical</u>														
<u>Uncertainty Only</u>														
Two jets sample	0.68	0.60	0.66	0.66	0.72	0.74	0.80	0.79	1.04	1.06	1.33	1.30	1.14	1.00
Combined sample	0.59	0.54	0.56	0.57	0.60	0.60	0.66	0.61	0.80	0.74	0.88	0.62	0.87	0.52
<u>All Uncertainties</u>														
Two jets sample	0.78	0.72	0.75	0.74	0.78	0.75	0.88	0.86	1.09	1.04	1.37	1.27	1.24	1.01
Combined sample	0.67	0.63	0.63	0.64	0.65	0.58	0.73	0.70	0.86	0.66	0.95	0.73	0.95	0.54

TABLE XII: Expected and measured 95% C.L. upper limits on the production cross section of left handed  $W'$  bosons. The two jets sample includes electron and muon, one and two tag samples. The combined sample includes all eight samples (electron and muon, one and two tag, two and three jets). The units are in pico barns.

	$W'$ (600 GeV)		$W'$ (650 GeV)		$W'$ (700 GeV)		$W'$ (750 GeV)		$W'$ (800 GeV)		$W'$ (850 GeV)		$W'$ (900 GeV)	
	Exp.	Obs.	Exp.	Obs.	Exp.	Obs.	Exp.	Obs.	Exp.	Obs.	Exp.	Obs.	Exp.	Obs.
<u>Statistical</u>														
<u>Uncertainty Only</u>														
Two jets sample	0.64	0.49	0.56	0.45	0.48	0.40	0.38	0.36	0.35	0.31	0.32	0.31	0.30	0.30
Combined sample	0.56	0.38	0.47	0.36	0.38	0.33	0.34	0.31	0.32	0.30	0.30	0.30	0.30	0.30
<u>All Uncertainties</u>														
Two jets sample	0.76	0.65	0.60	0.56	0.54	0.48	0.43	0.40	0.36	0.34	0.33	0.32	0.31	0.30
Combined sample	0.66	0.51	0.52	0.48	0.44	0.37	0.36	0.33	0.33	0.31	0.31	0.30	0.30	0.30

TABLE XIII: Expected and measured 95% C.L. upper limits on the production cross section of right handed  $W'$  bosons. The two jets sample includes electron and muon, one and two tag samples. The combined sample includes all eight samples (electron and muon, one and two tag, two and three jets). These also applicable to a left-handed  $W'_L$  if no interference with the SM is taken into account and  $M(\nu_R) < M(W'_R)$ . The units are in pico barns.

## IX. CONCLUSION

We search for  $W'$  boson production in the single top decay channel using  $0.9 \text{ fb}^{-1}$  of data taken by the DØ detector. We find no evidence for  $W'$  boson production and set 95% C.L. upper limits on the production cross-section for three different models of  $W'$  production. We compare our measurement to the theoretical prediction for the nominal value of the cross section to determine the lower limits on the mass of the  $W'$ . For a left-handed  $W'$  boson with SM-couplings and non-negligible interference with the SM  $W$  process, we set a limit of 775 GeV. For  $W'$  bosons with right-handed couplings (and for left-handed coupling when no interference with SM is included) we set a limit of 785 GeV, if  $M(\nu_R) < M(W')$ . For the case  $M(\nu_R) > M(W')$ , we set a limit of 810 GeV. We also put constraints on the  $W'$  gauge coupling and exclude couplings down to  $0.65g_{SM}$  for  $M(\nu_R) > M(W')$  and a  $W'$  mass of 600 GeV.

	$\sigma_{nom}$	$\sigma_{min}$	$\sigma_{max}$
with SM interference			
$M(W'_L) >$	775 GeV	744 GeV	821 GeV
without SM interference			
$M_\nu < M_{W'}$ : $M(W') >$	785 GeV	770 GeV	799 GeV
$M_\nu > M_{W'}$ : $M(W') >$	810 GeV	795 GeV	828 GeV

TABLE XIV: 95% C.L. lower limits on the mass of the  $W'$  for the nominal ( $\sigma_{nom}$ ), nominal- $1\sigma$  ( $\sigma_{min}$ ) and nominal+ $1\sigma$  ( $\sigma_{max}$ ) values of the theoretical cross section.

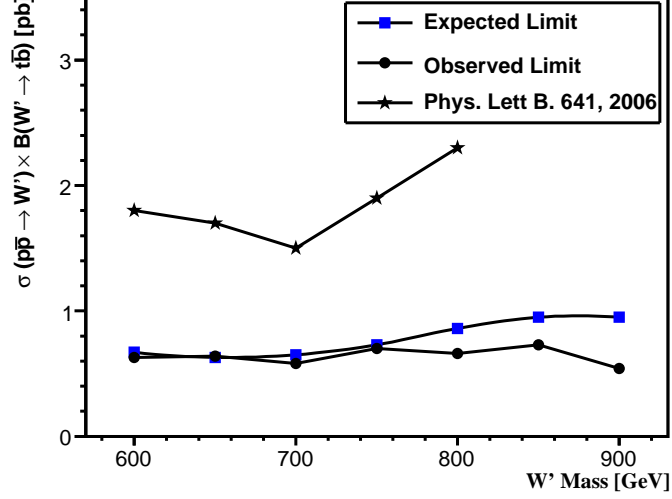


FIG. 8: Expected and observed limits for  $W'_L$  as a function of its mass, including interference effects with the SM. Also shown are observed limits from Ref. [31].

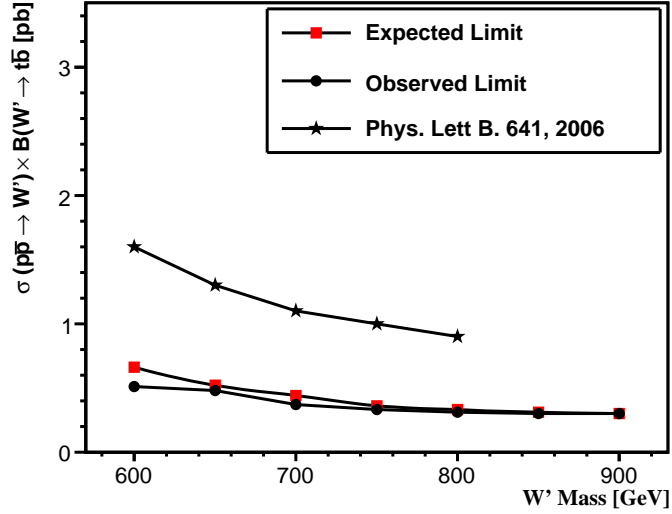


FIG. 9: Expected and observed limits for  $W'$  as a function of its mass. No interference with the SM are included. Also shown are observed limits from Ref. [31].

### Acknowledgments

We thank the single top group for providing the data samples and software used for this analysis. We have heavily relied on the ground work done by the single top group and without it this analysis would not have been possible in a timely fashion. We also thank Aran Garcia-Bellido, Ann Heinson, Ulrich Heintz, Shabnam Jabeen, and Reinhard

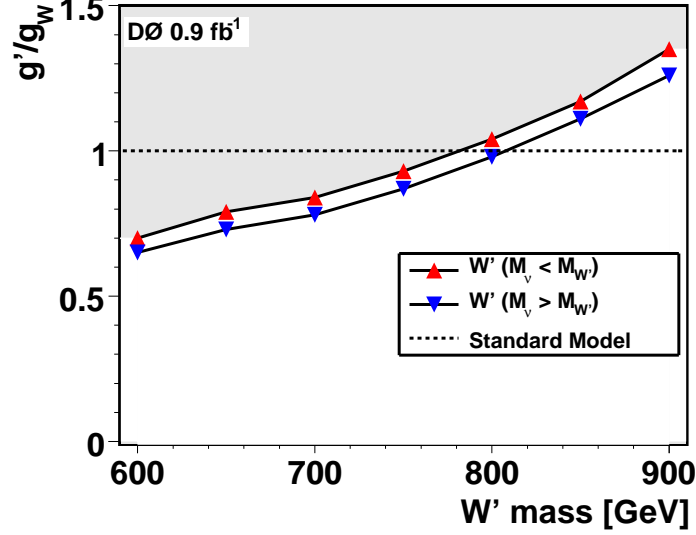


FIG. 10: Observed limits on the ratio of coupling constants,  $g'/g_{SM}$ . The points denoted by the red triangles correspond to the case  $M(\nu_R) < M(W')$  while the blue triangles are for the case  $M(\nu_R) > M(W')$ . No interference with the SM is included. The shaded region indicates coupling constants excluded by this analysis.

Swchwiehorst for many helpful hints and discussions.

- 
- [1] R. S. Chivukula, E. H. Simmons and J. Terning, Phys. Rev. D **53**, 5258 (1996).  
[2] D. B. Kaplan and H. Georgi, Phys. Lett. B **136**, 183 (1984).  
[3] H. Georgi and D. B. Kaplan, Phys. Lett. B **145**, 216 (1984).  
[4] N. Arkani-Hamed, A. G. Cohen and H. Georgi, Phys. Lett. B **513**, 232 (2001).  
[5] D. E. Kaplan and M. Schmaltz, JHEP **0310**, 039 (2003).  
[6] M. Schmaltz and D. Tucker-Smith, Ann. Rev. Nucl. Part. Sci. **55**, 229 (2005).  
[7] B. Schrempp, Proceedings of the 23rd International Conference on High Energy Physics, Berkeley (World Scientific, Singapore 1987);  
U. Baur *et al.*, Phys. Rev. **D35**, 297 (1987);  
M. Kuroda *et al.*, Nucl. Phys. **B261**, 432 (1985).  
[8] R.W. Robinett, Phys. Rev. **D26**, 2388 (1982);  
R.W. Robinett and J.L. Rosner, Phys. Rev. **D26**, 2396 (1982);  
P. Langacker, R. W. Robinett, and J.L. Rosner, Phys. Rev. **D30**, 1470 (1984).  
[9] M. Cvetič and P. Langacker, Mod. Phys. Lett. A **11**, 1247 (1996).  
[10] J. C. Pati, arXiv:hep-ph/0606089.  
[11] M. Green and J. Schwarz, Phys. Lett. **149B**, 117(1984);  
D. Gross *et al.*, Phys. Rev. Lett. **54**, 502 (1985);  
E. Witten, Phys. Lett. **155B**, 1551 (1985);  
P. Candelas *et al.*, Nucl. Phys. **B258**, 46 (1985);  
M. Dine *et al.*, Nucl. Phys. **B259**, 549 (1985).  
[12] A. Datta, P. J. O'Donnell, Z. H. Lin, X. Zhang and T. Huang, Phys. Lett. B **483**, 203 (2000).  
[13] R. Sundrum, arXiv:hep-th/0508134;  
C. Csaki, Jay Hubisz, Patrick Meade, arXiv:hep-ph/0510275;  
G. Kribs, arXiv:hep-ph/0605325.  
[14] E. Malkawi, T. Tait and C. P. Yuan, Phys. Lett. B **385**, 304 (1996).  
[15] D. J. Muller and S. Nandi, Phys. Lett. B **383**, 345 (1996).  
[16] J. C. Pati and A. Salam, Phys. Rev. D **10**, 275 (1974).  
[17] R. N. Mohapatra and J. C. Pati, Phys. Rev. D **11**, 566 (1975).  
[18] R. N. Mohapatra and J. C. Pati, Phys. Rev. D **11**, 2558 (1975).  
[19] G. Senjanovic and R. N. Mohapatra, Phys. Rev. D **12**, 1502 (1975).

- [20] Y. Mimura and S. Nandi, Phys. Lett. B **538**, 406 (2002).
- [21] M. Cvetič and J. C. Pati, Phys. Lett. B **135**, 57 (1984).
- [22] P. Langacker and S. Uma Sankar, Phys. Rev. D **40**, 1569 (1989).
- [23] J. Donoghue and B. Holstein, Phys. Lett. **113B**, 383 (1982);
- [24] L. Wolfenstein, Phys. Rev. D **29**, 2130 (1984).
- [25] W.-M. Yao et al., J. Phys. G **33**, 1 (2006).
- [26] D0 Collaboration, V. Abazov *et al.*, Phys. Rev. D **69**, 111101 (2004).
- [27] CDF Collaboration, T. Affolder *et al.*, Phys. Rev. Lett. **87**, 231803 (2001).
- [28] CDF Collaboration, D. Acosta *et al.*, Phys. Rev. Lett. **90**, 081802 (2003).
- [29] E. H. Simmons, Phys. Rev. D **55**, 5494 (1997).
- [30] E. Boos, V. Bunichev, L. Dudko and M. Perfilov, Phys. Lett. B **655**, 245 (2007) [arXiv:hep-ph/0610080].
- [31] V.M. Abazov *et al.*, “Search for  $W'$  boson production in the top quark decay channel”, Phys. Lett. B **641**, 423-431 (2006);  
R. Schwienhorst *et al.* “Search for  $W'$  production in the single top quark decay channel at DØ in Run II”, DØ Note 5002.
- [32] V.M. Abazov *et al.*, (DØ Collaboration), “The upgraded DØ detector,” Nucl. Instrum. Methods Phys. Res. A **565**, 463 (2006).
- [33] DØ Collaboration, S. Abachi *et al.*, Nucl. Instrum. Methods Phys. Res. A **338**, 185 (1994).
- [34] V. M. Abazov *et al.*, “Evidence for Production of Single Top Quarks and First Direct Measurement of  $|V_{tb}|$ ”, *Phys. Rev. Lett.* **98**, 18 (2007).
- [35] E. Aguiló *et al.* (D0 Single Top Group), “Search for the Single Top Quark Production in 1 fb<sup>-1</sup> of Data”, D0Note 5285 (2006).
- [36] A. Schwartzman and C. Tully, “Primary Vertex Reconstruction by Means of Adaptive Vertex Fitting” D0 Note 4918 (2005).
- [37] T. Gadfort *et al.*, “Muon Identification Certification for p17 Data” D0 Note 5157 (2006).
- [38] G. Blazey *et al.* “Run II Jet Physics” D0 Note 3750 (2000).
- [39] “Preliminary p17 JES for Data and MC (JetCorr v07-01-02)”  
[http://www-d0.fnal.gov/phys\\_id/jes/d0\\_private/certified/certified\\_jes.html](http://www-d0.fnal.gov/phys_id/jes/d0_private/certified/certified_jes.html).
- [40] A. Harel, “Jet ID Optimization” D0 Note 4919 (2006).
- [41] The method is described for p14 in: N. Makovec and J.-F. Grivaz, “Shifting, Smearing and Removing Simulated Jets,” DØ Note 4914 (2005). Application of the method in p17 can be seen here: <http://www-d0.hef.kun.nl//fullAgenda.php?ida=a06904&fid=32>.
- [42] M. Anastasoie, S. Robinson, and T. Scanlon “Performance of the NN b-Tagging Tool on p17 Data” D0 Note 5213 (2006).
- [43] Data Quality Group web page: [http://www-d0.fnal.gov/computing/data\\_quality/d0\\_private/forusers.html](http://www-d0.fnal.gov/computing/data_quality/d0_private/forusers.html).
- [44] E. Boos *et al.* [CompHEP Collaboration], Nucl. Instrum. Meth. A **534**, 250 (2004) [arXiv:hep-ph/0403113].
- [45] E. E. Boos, V. E. Bunichev, L. V. Dudko, V. I. Savrin and A. V. Sherstnev, Phys. Atom. Nucl. **69**, 1317 (2006) [Yad. Fiz. **69**, 1352 (2006)].
- [46] Z. Sullivan, Phys. Rev. D **66**, 075011 (2002).
- [47] B.W. Harris, E. Laenen, L. Phaf, Z. Sullivan, and S. Weinzierl, Phys. Rev. D **66**, 054024 (2002).
- [48] Z. Sullivan, Phys. Rev. D **70**, 114012 (2004).
- [49] J. Campbell, R.K. Ellis, and F. Tramontano, Phys. Rev. D **70**, 094012 (2004).
- [50] Q.H. Cao, R. Schwienhorst, and C.-P. Yuan, Phys. Rev. D **71**, 054023 (2005).
- [51] T.Sjostrand *et al.*, arXiv:hep-ph/0108264.
- [52] R. Brun *et al.*, CERN Program Library Long Writeup **W** 5013 (1994).
- [53] M.L.Mangano *et al.* J. High Energy Phys. **0307**, 001 (2003).
- [54] N. Kidonakis and R.Vogt, Phys. Rev. D **68**, 114014 (2003).
- [55] S. Jain *et al.*, “Limits using a Bayesian approach in the package 'top\_statistics'”, D0Note 5123 (2006).
- [56] CDF Collaboration,  $W'$ -like Resonances in the  $t\bar{b}$  Decay Channel with 1 fb<sup>-1</sup>, CDF Note 8747 (2007).
- [57] The mixing angle  $\zeta$  is usually constrained to be small in models where the  $W$  and the  $W'$  mix [23, 24] and therefore such searches are well motivated.

## APPENDIX A: SYSTEMATIC UNCERTAINTIES

	Single-Tagged Electron Channel Percentage Errors								
	$W'$	$tb$	$tqb$	$tllj$	$tll$	$Wbb$	$Wcc$	$Wjj$	Multijet
Luminosity	6.1	6.1	6.1	6.1	6.1	—	—	—	—
Cross section	—	16.0	15.0	18.0	18.0	—	—	—	—
Branching fraction	1.0	1.0	1.0	1.0	1.0	—	—	—	—
Matrix method	—	—	—	—	—	16.8	16.8	16.8	16.8
Primary vertex	2.4	2.4	2.4	2.4	2.4	—	—	—	—
Electron ID	5.5	5.5	5.5	5.5	5.5	—	—	—	—
Jet ID	1.5	1.5	1.5	1.5	1.5	—	—	—	—
Jet fragmentation	5.0	5.0	5.0	7.0	5.0	—	—	—	—
Trigger	3.0	3.0	3.0	3.0	3.0	—	—	—	—
Components for Normalization and Shape									
Jet energy scale	4.1(4.8)	5.3	5.8	4.1	3.2	—	—	—	—
Flavor-dependent TRFs	1.9(1.9)	2.1	4.5	2.9	2.1	4.4	6.2	7.6	—

TABLE XV: Electron channel uncertainties, requiring exactly one tag and exactly three jets.  $W'$  shape uncertainties include numbers for both  $W'_R$  and  $W'_L$  (in parenthesis).

	Double-Tagged Electron Channel Percentage Errors								
	$W'$	$tb$	$tqb$	$tllj$	$tll$	$Wbb$	$Wcc$	$Wjj$	Multijet
Luminosity	6.1	6.1	6.1	6.1	6.1	—	—	—	—
Cross section	—	16.0	15.0	18.0	18.0	—	—	—	—
Branching fraction	1.0	1.0	1.0	1.0	1.0	—	—	—	—
Matrix method	—	—	—	—	—	22.1	22.1	22.1	22.1
Primary vertex	2.4	2.4	2.4	2.4	2.4	—	—	—	—
Electron ID	5.5	5.5	5.5	5.5	5.5	—	—	—	—
Jet ID	1.5	1.5	1.5	1.5	1.5	—	—	—	—
Jet fragmentation	5.0	5.0	5.0	7.0	5.0	—	—	—	—
Trigger	3.0	3.0	3.0	3.0	3.0	—	—	—	—
Components for Normalization and Shape									
Jet energy scale	4.3(3.5)	4.8	4.0	3.5	2.9	—	—	—	—
Flavor-dependent TRFs	13.4(13.5)	12.7	12.4	12.6	12.8	12.0	13.3	16.4	—

TABLE XVI: Electron channel uncertainties, requiring exactly two tags and exactly three jets.  $W'$  shape uncertainties include numbers for both  $W'_R$  and  $W'_L$  (in parenthesis).

	Single-Tagged Muon Channel Percentage Errors								
	$W'$	$tb$	$tqb$	$tllj$	$tll$	$Wbb$	$Wcc$	$Wjj$	Multijet
Luminosity	6.1	6.1	6.1	6.1	6.1	—	—	—	—
Cross section	—	16.0	15.0	18.0	18.0	—	—	—	—
Branching fraction	1.0	1.0	1.0	1.0	1.0	—	—	—	—
Matrix method	—	—	—	—	—	20.8	20.8	20.8	20.8
Primary vertex	3.0	3.0	3.0	3.0	3.0	—	—	—	—
Muon ID	7.4	7.4	7.4	7.4	7.4	—	—	—	—
Jet ID	1.5	1.5	1.5	1.5	1.5	—	—	—	—
Jet fragmentation	5.0	5.0	5.0	7.0	5.0	—	—	—	—
Trigger	6.0	6.0	6.0	6.0	6.0	—	—	—	—
Components for Normalization and Shape									
Jet energy scale	10.8(8.9)	9.3	9.0	10.8	7.6	—	—	—	—
Flavor-dependent TRFs	1.6(1.6)	1.8	4.4	2.6	1.9	4.3	6.2	7.6	—

TABLE XVII: Muon channel uncertainties, requiring exactly one tag and exactly three jets.  $W'$  shape uncertainties include numbers for both  $W'_R$  and  $W'_L$  (in parenthesis).

	Double-Tagged Muon Channel Percentage Errors								
	$W'$	$tb$	$tqb$	$t\bar{l}j$	$t\bar{l}l$	$Wbb$	$Wcc$	$Wjj$	Multijet
Luminosity	6.1	6.1	6.1	6.1	6.1	—	—	—	—
Cross section	—	16.0	15.0	18.0	18.0	—	—	—	—
Branching fraction	1.0	1.0	1.0	1.0	1.0	—	—	—	—
Matrix method	—	—	—	—	—	25.0	25.0	25.0	25.0
Primary vertex	3.0	3.0	3.0	3.0	3.0	—	—	—	—
Muon ID	7.4	7.4	7.4	7.4	7.4	—	—	—	—
Jet ID	1.5	1.5	1.5	1.5	1.5	—	—	—	—
Jet fragmentation	5.0	5.0	5.0	7.0	5.0	—	—	—	—
Trigger	6.0	6.0	6.0	6.0	6.0	—	—	—	—
Components for Normalization and Shape									
Jet energy scale	10.8(10.0)	10.2	7.6	10.1	7.8	—	—	—	—
Flavor-dependent TRFs	13.3(13.3)	12.6	12.3	12.4	12.7	12.0	13.1	16.4	—

TABLE XVIII: Muon channel uncertainties, requiring exactly two tags and exactly three jets.  $W'$  shape uncertainties include numbers for both  $W'_R$  and  $W'_L$  (in parenthesis).

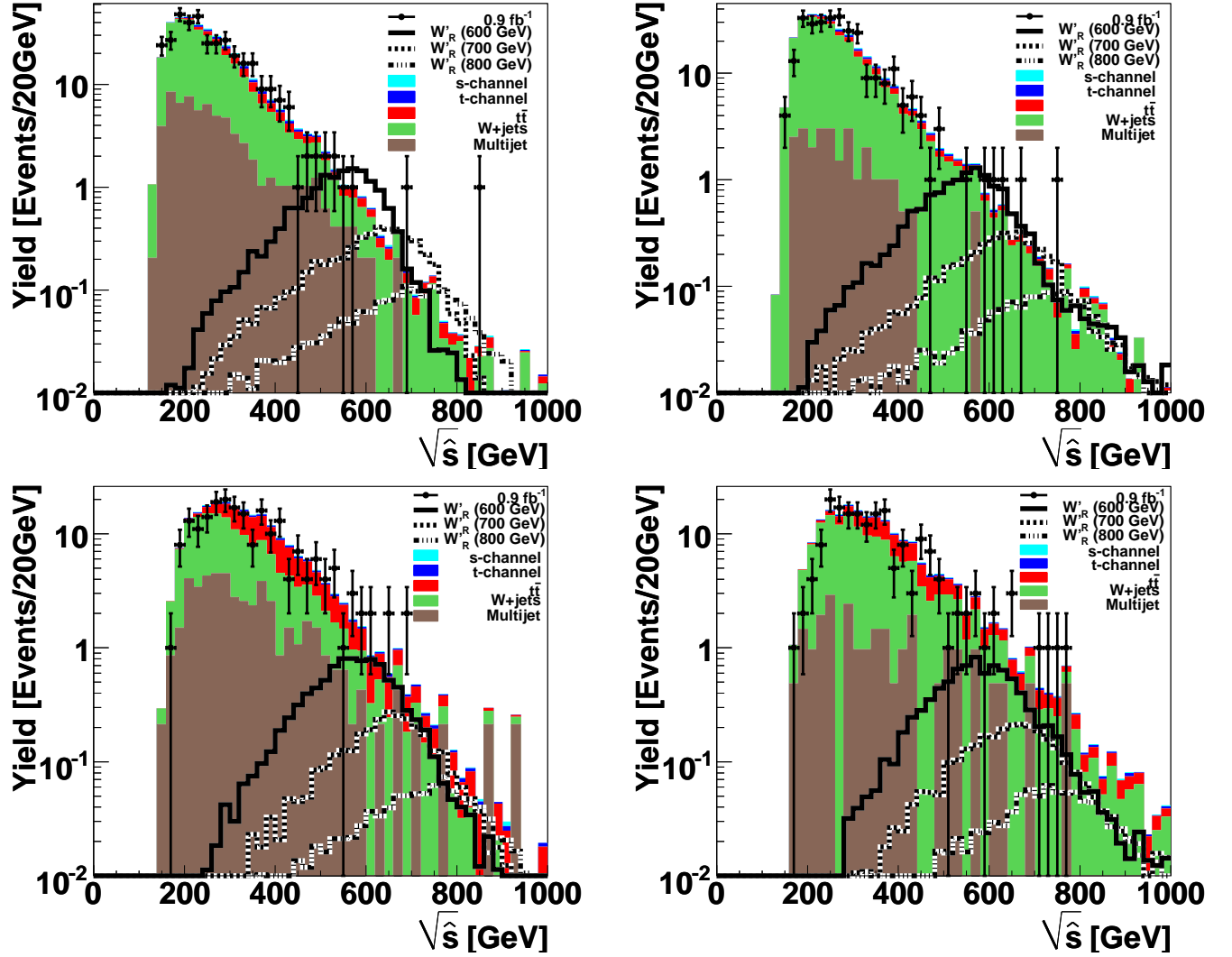


FIG. 11: Reconstructed  $W'$  invariant mass distributions for data, background and three different  $W'_R$  signal mass points for events with one  $b$ -tagged jet. The plots in the top (bottom) row are for events with two (three) jets. Events with electrons (muons) are shown on the left (right).

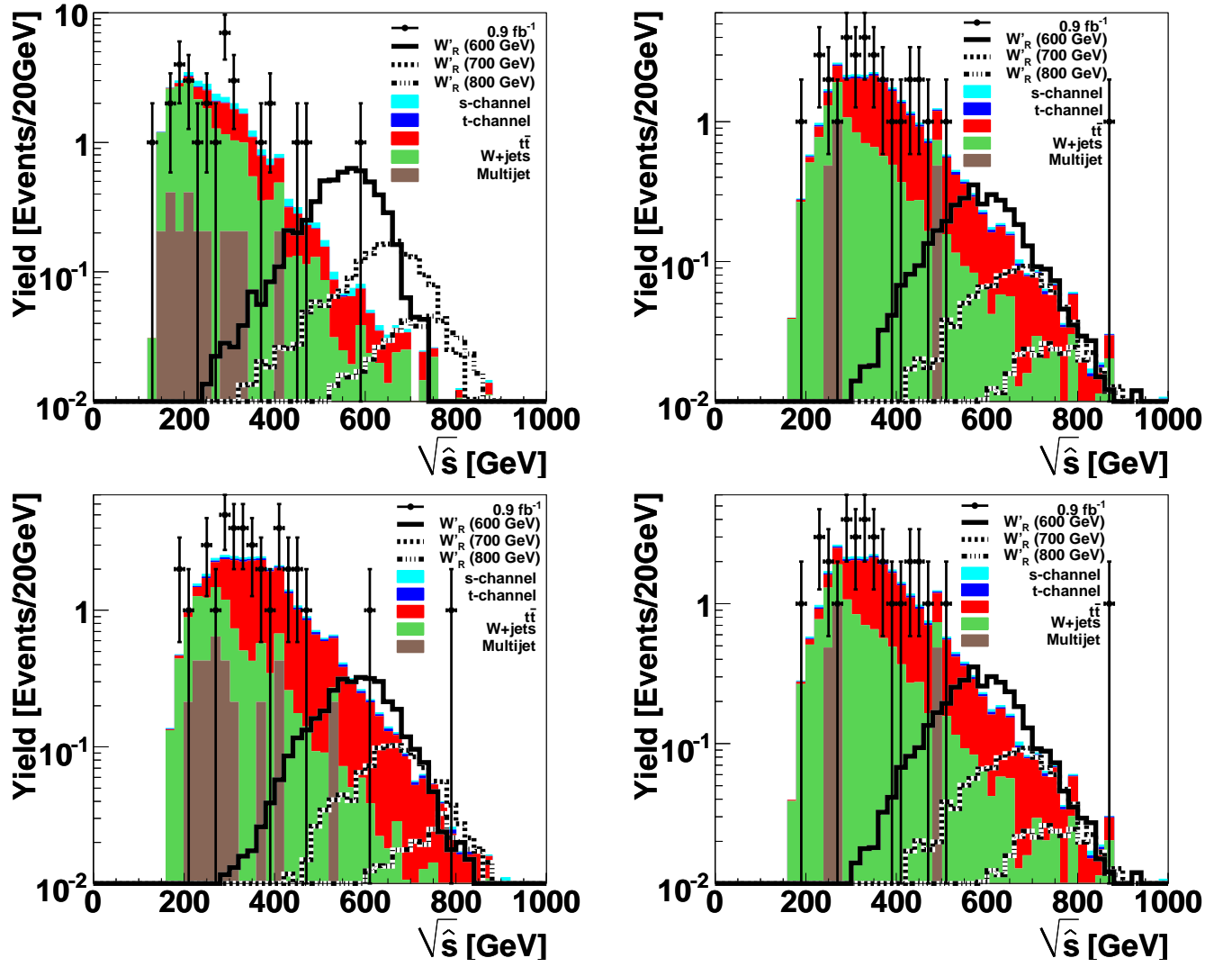


FIG. 12: Reconstructed  $W'$  invariant mass distributions for data, background and three different  $W'_R$  signal mass points for events with two  $b$ -tagged jets. The plots in the top (bottom) row are for events with two (three) jets. Events with electrons (muons) are shown on the left (right).

